Memory effect in photochromic rare-earth oxyhydride thin films studied by in situ positron annihilation spectroscopy upon photodarkening-bleaching cycling

Wu, Ziying; De Wit, Lidwin; Beek, Melanie; Colombi, Giorgio; Chaykina, Diana; Schreuders, Herman; Schut, Henk; Butterling, Maik; Brück, Ekkes; Dam, Bernard

DOI
10.1103/PhysRevMaterials.8.045201

Publication date
2024

Document Version
Final published version

Published in
Physical Review Materials

Citation (APA)
Wu, Z., De Wit, L., Beek, M., Colombi, G., Chaykina, D., Schreuders, H., Schut, H., Butterling, M., Brück, E., Dam, B., & Eijt, S. W. H. (2024). Memory effect in photochromic rare-earth oxyhydride thin films studied by in situ positron annihilation spectroscopy upon photodarkening-bleaching cycling. *Physical Review Materials*, *8*(4), Article 045201. https://doi.org/10.1103/PhysRevMaterials.8.045201

PHYSICAL REVIEW MATERIALS **8**, 045201 (2024)

Memory effect in photochromic rare-earth oxyhydride thin films studied by *in situ* positron annihilation spectroscopy upon photodarkening-bleaching cycling

Ziying Wu,[1,*] Lidwin de Wit,[1] Melanie Beek,[1] Giorgio Colombi,[2] Diana Chaykina,[1,2] Herman Schreuders,[2]
Henk Schut,[3] Maciej Oskar Liedke,[4] Maik Butterling,[4] Andreas Wagner,[4] Marcel Dickmann,[5]
Ekkes Brück,[1] Bernard Dam,[2] and Stephan W. H. Eijt[1]

[1] *Fundamental Aspects of Materials and Energy, Department of Radiation Science and Technology, Faculty of Applied Sciences, Delft University of Technology, Mekelweg 15, NL-2629 JB Delft, The Netherlands*
[2] *Materials for Energy Conversion and Storage, Department of Chemical Engineering, Faculty of Applied Sciences, Delft University of Technology, Van der Maasweg 9, NL-2629 HZ Delft, The Netherlands*
[3] *Neutron and Positron Methods for Materials, Department of Radiation Science and Technology, Faculty of Applied Sciences, Delft University of Technology, Mekelweg 15, NL-2629 JB Delft, The Netherlands*
[4] *Institute of Radiation Physics, Helmholtz-Zentrum Dresden-Rossendorf, Bautzner Landstrasse 400, D-01328 Dresden, Germany*
[5] *Institut für angewandte Physik und Messtechnik, Bundeswehr Universität München, D-85579 Neubiberg, Germany*

(Received 18 December 2023; revised 8 March 2024; accepted 13 March 2024; published 15 April 2024)

Cycling stability of the photochromic effect in rare-earth oxyhydride thin films is of great importance for long-term applications such as smart windows. However, an increasingly slower bleaching rate upon photochromic cycling was found in yttrium oxyhydride thin films; the origin of this memory effect is yet unclear. In this work, the microstructural changes under six photodarkening-bleaching cycles in YH_xO_y and GdH_xO_y thin films are investigated by *in situ* illumination Doppler broadening positron annihilation spectroscopy, complemented by positron annihilation lifetime spectroscopy (PALS) investigations on YH_xO_y films before and after one cycle. For the first three cycles, the Doppler broadening S parameter after bleaching increases systematically with photodarkening-bleaching cycle, and correlates with the bleaching time constant extracted from optical transmittance measurements. This suggests that the microstructural evolution that leads to progressively slower bleaching involves vacancy creation and agglomeration. PALS suggests that during a photodarkening-bleaching cycle, divacancies are formed that are possibly composed of illumination-induced hydrogen vacancies and preexisting yttrium monovacancies, and vacancy clusters grow, which might be due to local removal of hydrogen. If bleaching is a diffusion-related process, the formed vacancy defects induced by illumination might affect the diffusion time by reducing the diffusion coefficient. Hydrogen loss could also be a key factor in the reduced bleaching kinetics. Other microstructural origins including domain growth, or formation of OH^- hydroxide groups, are also discussed with respect to the slower bleaching kinetics. During the fourth to sixth photodarkening-bleaching cycle, reversible shifts in the Doppler S and W parameters are seen that are consistent with the reversible formation of metallic-like domains, previously proposed as a key factor in the mechanism for the photochromic effect.

DOI: 10.1103/PhysRevMaterials.8.045201

I. INTRODUCTION

Rare-earth oxyhydride thin films have gained increasing interest due to their color-neutral photochromic effect at room temperature. Their photochromic performance in terms of contrast and bleaching speed can be modified by different strategies, such as adjusting the type of cation, tuning the deposition pressure, thermal annealing, and doping, making them promising for applications in smart windows and photochromic sunglasses [1–5]. A stable photochromic performance during photodarkening-bleaching cycles and fast switching kinetics is required for long-term practical applications. However, a progressively slower bleaching kinetics upon photochromic cycling was observed in yttrium oxyhydride (YH_xO_y) thin films [6]. This is the so-called memory effect, which is induced by the illumination. This memory effect remains for timescales on the order of at least a few weeks in YH_xO_y [6]. The memory effect is therefore a major concern in view of practical applications, and understanding its origin is of great importance.

However, the microscopic origins of the memory effect have not been unraveled yet. Many previous studies have focused on the nature of the reversible processes and optical phenomena linked to the photochromism, while the link of light-induced irreversible changes to the memory effect has rarely been reported. Moldarev *et al.* [7] observed the release of hydrogen gas during illumination for the first two cycles and their results suggest that the removal of hydrogen may be related to the memory effect. Our previous positron annihilation studies during one photodarkening-bleaching cycle showed irreversible shifts in Doppler broadening parameters that maintained after full bleaching in both YH_xO_y and GdH_xO_y films, suggesting that stable or weakly

---

[*] Corresponding author: Z.Wu-2@tudelft.nl

2475-9953/2024/8(4)/045201(14)

metastable vacancy-related defects are formed, which may contribute to the memory effect and/or are related to the microscopic origins of the memory effect [8–10]. In order to gain understanding of the memory effect, further exploration of the microstructural changes upon cycling is required.

Positron annihilation spectroscopy (PAS) is a well-established nondestructive tool to characterize open-volume defects on a nanometer scale in solids [11–14]. The neutral and negatively charged open-volume defects are often effective positron traps due to the lack of positive-ion cores. By measuring the Doppler shifts of the positron-electron annihilation photopeak, one can obtain information on changes in the local valence electron states via the positron-electron momentum distribution caused by changes in open-volume defects and electronic structure. This technique is known as Doppler-broadening positron annihilation spectroscopy (DB-PAS). Another well-known positron annihilation technique is positron annihilation lifetime spectroscopy (PALS), which can quantify and identify open-volume defects to provide information on the type and concentration of vacancy defects. Namely, the lifetime of a positron in an open-volume defect will be longer than in the defect-free material, since the electron density in the open volume defect is lower, leading to a reduction in the positron-electron annihilation rate.

In this work, the photochromic performance of YH_xO_y and GdH_xO_y thin films under six photodarkening-bleaching cycles is monitored by *in situ* transmittance measurements, and the microstructural changes under the same six cycles are examined by *in situ* illumination DB-PAS, complemented by PALS investigations on YH_xO_y thin films before and after one cycle. The *in situ* DB-PAS study demonstrates that the increase of the bleaching-time constant upon cycling is accompanied by an increase of the S parameter after bleaching, revealing a strong correlation between these parameters. The observed increase in S parameter is attributed to vacancy agglomeration of light-induced hydrogen vacancies with yttrium monovacancies and growth of vacancy clusters present in the as-deposited films, as revealed by PALS measurements before and after one photodarkening-bleaching cycle. These findings suggest that incomplete refilling of the light-created hydrogen vacancies with hydrogen could be a key ingredient of the microscopic origin of the memory effect.

II. EXPERIMENT

A. Sample preparation

A total of eight yttrium oxyhydride films and eight gadolinium oxyhydride thin films were prepared by two steps. First, metal hydride films were deposited on fused-silica substrates by reactive magnetron sputtering with a constant Ar/H_2 flow (7:1) at room temperature. The deposition power supplied to the yttrium and gadolinium targets was 100 and 165 W, respectively. The total pressure was maintained at 0.5 Pa for YH_xO_y and at 0.8 Pa for GdH_xO_y, respectively, which exceeded the critical pressure necessary to induce sufficient porosity of the metal hydride films, enabling the subsequent formation of the semiconducting YH_xO_y and GdH_xO_y oxyhydride phase during postoxidation [1]. This postoxidation process occurs by exposure of the metal hydride films to ambient environment, in which an oxidation time of ∼10 days is sufficient to achieve a stable composition. After that, half of the yttrium oxyhydride and gadolinium oxyhydride thin-film samples of each batch were stored in ambient air (noted as YHO-air and GdHO-air), while the others were stored under a vacuum pressure of 10^{-2} mbar (noted as YHO-vac and GdHO-vac). The thickness of the YH_xO_y and GdH_xO_y films was determined by profilometry to be 420 and 570 nm, respectively, within ∼10% accuracy. For the PALS measurements, one additional thin-film YH_xO_y sample was made by the same recipe while the other was deposited at 200 W. The thickness of the two additional YH_xO_y films was determined to be ∼370 nm. Table I summarizes the different types of rare-earth oxyhydride thin films studied in this work as well as the corresponding deposition parameters, thickness, and storage environment.

B. Characterization

The transmittance spectra of the yttrium and gadolinium oxyhydride film samples were acquired in the range of 230–1120 nm on a custom-built optical fiber-based spectrometer [2]. The optical properties of the vacuum-stored samples were measured under a vacuum condition of 8–9 Pa. The photochromic effect of oxyhydride films was triggered by a narrow-wavelength light-emitting diode (385 nm) with an intensity of ∼30 mW/cm^2. The same light source equipped with a Köhler lens system was used to illuminate the sample for the *ex-situ* illumination x-ray diffraction (XRD) and the *in situ* illumination DB-PAS experiments. For all photodarkening-bleaching cycles, the illumination time and the monitoring time during bleaching were set at, respectively, 2.5 and 20 h, for both the optical and DB-PAS measurements, meaning that a full photodarkening-bleaching cycle corresponded to 22.5 h.

The grazing-incidence x-ray-diffraction patterns were collected on a PANalytical X'Pert PRO diffractometer at an incident angle of 2 ° with a Cu $K\alpha$ source ($\lambda = 1.54$ Å) at room temperature.

DB-PAS experiments were carried out using the variable-energy positron (VEP) beam setup at the TU Delft Reactor Institute [15]. The intensity of the positron beam at sample position was around 10^4 e^+/s and the full width at half maximum (FWHM) of the beam diameter was around 8 mm. The low-momentum shape (S) and high-momentum wing (W) parameters were defined as the annihilation events (1) in the central area with an energy window of $|E| < 0.77$ keV (or electron momentum $|p| < 3.0 \times 10^{-3}$ m_0c) and (2) the area with an energy window of $2\,\text{keV} < |E| < 6$ keV(8.2×10^{-3} $m_0c < |p| < 23.4 \times 10^{-3}$ m_0c), divided by the total annihilation events under the gamma-ray photopeak around 511 keV. The S parameter reflects the annihilation with primarily valence electrons, providing sensitivity to the electronic structure and the presence of vacancies, while the W parameter represents positron annihilation with semicore electrons, providing sensitivity to the local chemical surrounding of the positron trapping site. The collected depth profiles with implantation energies of 0.1–25 keV were fitted by VEPFIT to extract the S and W parameters of the rare-earth oxyhydride layer [16]. For the time-dependent *in situ* DB-PAS measurements under multiple illumination cycles, the implantation energy of positrons is fixed at 5.5 and 10 keV for YH_xO_y and GdH_xO_y, respectively, to ensure that most of the positrons

TABLE I. List of the main parameters and measurements of rare-earth oxyhydride thin-film samples studied in this work.

Sample type	Total deposition pressure (Pa)	Deposition power (W)	Thickness (nm)	Storage environment	Measurements
YHO-air	0.5	100	420	Air	Transmittance, DB-PAS, XRD
YHO-vac	0.5	100	420	Vacuum	Transmittance, DB-PAS
GdHO-air	0.8	165	570	Air	Transmittance, DB-PAS, XRD
GdHO-vac	0.8	165	570	Vacuum	Transmittance, DB-PAS
YHO-1	0.5	100	370	Air	PALS
YHO-2	0.5	200	370	Air	PALS

annihilate in the oxyhydride layer (>95% for YH_xO_y and >90% GdH_xO_y) rather than in the substrate or at the surface. The fractions of positrons annihilating in each layer of YH_xO_y and GdH_xO_y extracted from the VEPFIT analyses are shown in Appendix A. The positron implantation depth distribution is assumed to follow a Makhovian implantation profile. The calculated Makhovian implantation profiles for an implantation energy of 5.5 keV for YH_xO_y and of 10 keV for GdH_xO_y are plotted in Fig. 1, which demonstrates that these implantation profiles fit well within the thickness of the layers (see Table I). The positron implantation profiles in a material with density ρ in g/cm^3 are described by

$$P\,(z,\ E) = \frac{mz^{m-1}}{{z_0}^m}\exp\left[-\left(\frac{z}{z_0}\right)^m\right], \qquad (1)$$

with $m = 2$, $z =$ the implantation depth, and $z_0 = 1.13\bar{z}$, with $\bar{z}$ the mean implantation depth in nanometers, is a function of the positron implantation energy E in keV according to $z_0(E) = \frac{AE^n}{\rho}$, and we used $n = 1.6$ and $A = 4\,\mu\text{g}\,\text{cm}^{-2}\,\text{keV}^{-n}$ [17,18], and $\rho = 4.3\,\text{g/cm}^3$ for YH_xO_y and $\rho = 7.2\,\text{g/cm}^3$ for GdH_xO_y, respectively.

PALS measurements were performed using the Monoenergetic Positron Spectroscopy (MePS) setup at the ELBE (Electron Linac for beams with high Brilliance and low Emittance) facility at the Helmholtz-Zentrum Dresden-Rossendorf (HZDR), Germany [19]. Approximately 10^7 counts were collected for each spectrum. A $CeBr_3$ scintillator detector coupled to a Hamamatsu R13089-100 photomultiplier tube was utilized for gamma quanta acquisition and the signals were processed by the SPDevices ADQ14DC-2X digitizer (14-bit vertical resolution and 2 GS/s horizontal resolution) [20]. The time resolution was estimated to be ∼250 ps by determination of the PALS spectrum of a reference amorphous yttria stabilized zirconia sample with two lifetime components. Since the thickness of the YH_xO_y films (∼370 nm) examined in the PALS study was slightly less than the thickness of the YH_xO_y films studied in the DB-PAS experiments, the positron implantation energy was fixed to 5 keV before illumination and during the photodarkening-bleaching cycle. The corresponding calculated Makhovian positron implantation profile is shown in Fig. 1. The program PALSFIT3 was used to analyze the positron lifetime spectra [21].

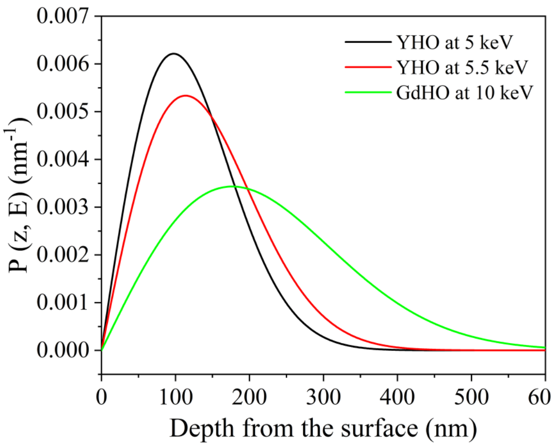

FIG. 1. Positron implantation profiles for implantation energies of 5 and 5.5 keV in YH_xO_y, and 10 keV in GdH_xO_y.

III. RESULTS

A. Photochromic responses upon cycling

Figure 2 shows the transmittance averaged over the wavelength range of 450 to 1000 nm as a function of time upon six consecutive photodarkening-bleaching cycles for four thin-film samples: YHO-air, YHO-vac, GdHO-air, and GdHO-vac. The transmittance in the photodarkened state after each illumination period of 2.5 h is fairly constant for the six cycles for each film, and there is no significant difference in transmit-

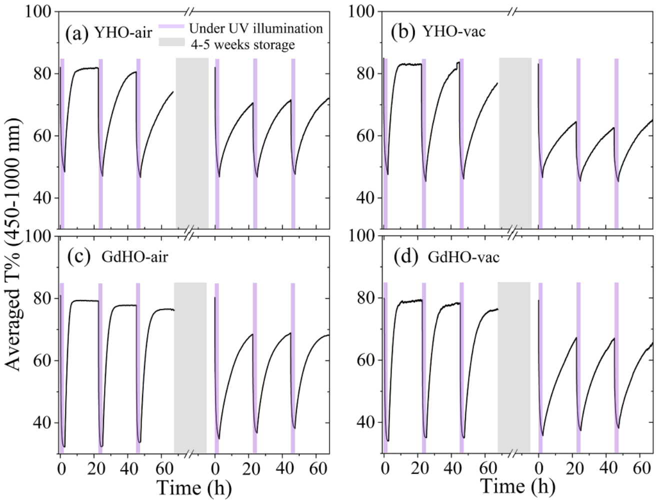

FIG. 2. Time dependence of average transmittance in the range of 450–1000 nm of (a) YHO-air, (b) YHO-vac, (c) GdHO-air, and (d) GdHO-vac thin films during six photodarkening(purple shaded region)-bleaching cycles including an intermediate period of 4–5 weeks of storage in air or vacuum (shaded with a rectangular gray area).

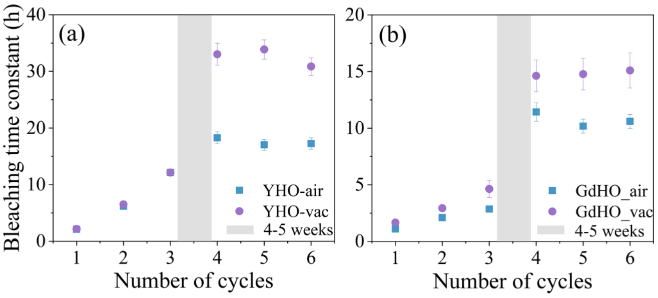

FIG. 3. The bleaching-time constant τ_{bleach} extracted from the optical transmittance measurements according to Eq. (1) for the (a) YH_xO_y and (b) GdH_xO_y films with the number of cycles.

tance between air-stored and vacuum-stored films, as can been seen comparing Figs. 2(a) to 2(b) and 2(c) to 2(d), respectively. However, the bleaching process becomes progressively slower with subsequent photodarkening-bleaching cycle, i.e., longer time is needed to reverse back to the bleached (transparent) state for the first four cycles, after which the bleaching rate stabilizes. This process of increasingly slower bleaching kinetics in YH_xO_y films upon photochromic cycling is known as the memory effect [6]. Quantitatively, the bleaching process can be evaluated by the bleaching-time constant (τ_{bleach}), which can be determined according to Eq. (2), assuming first-order kinetics for the bleaching process [4]. The corresponding fits are shown in Appendix B, and the extracting values for bleaching-time constant for each cycle are shown in Fig. 3.

$$\ln\left(-\ln\left(\frac{T(t)}{T_0}\right)\right) = -\frac{1}{\tau_{\text{bleach}}}t + \ln\left(-\ln\left(\frac{T_{\text{dark}}}{T_0}\right)\right), \qquad (2)$$

where T_0 is the initial average transmittance before illumination, T_{dark} is the transmittance of the photodarkened state at the end of the illumination period, and $T(t)$ is the transmittance after a time t of bleaching.

As shown in Fig. 3, τ_{bleach} increases almost linearly for the first three cycles for all samples, in which τ_{bleach} shows an increase by a factor of ~6 and ~2 for YH_xO_y and GdH_xO_y, respectively. After the storage under dark conditions for 4–5 weeks and the subsequent fourth illumination, the bleaching process is even slower (larger τ_{bleach}) compared to the previous cycle, demonstrating that the memory effect remains present for at least 4–5 weeks of storage, both under ambient or vacuum conditions. After the fourth photodarkening-bleaching cycle, the bleaching time τ_{bleach} remains constant on subsequent cycling. Clearly, faster bleaching is observed in the GdH_xO_y films compared to the YH_xO_y films, consistent with previous studies, that connected the faster bleaching kinetics to the larger ionic radius of Gd compared to Y and Sc [2]. In addition, the similarity of the evolution of the photochromic effect observed in the oxyhydride films stored and measured in air and in vacuum, as shown in Figs. 2 and 3, indicates that an ambient environment is not a crucial factor for the photochromic effect, consistent with Ref. [7] where it was shown that YH_xO_y bleaches under ultrahigh-vacuum conditions. However, we do observe that both YH_xO_y and GdH_xO_y films bleach slower after four weeks of storage under vacuum compared to four weeks of storage in air.

B. Microstructural changes investigated by *in situ* illumination positron annihilation

In order to gain an understanding of the origin of the memory effect from a microstructural perspective, *in situ* DB-PAS measurements were conducted during six photodarkening-bleaching cycles with time intervals for illumination and for monitoring during bleaching that are the same as for the transmittance measurements reported in Sec. III A. The evolution of the line-shape parameter S as a function of time for six photodarkening-bleaching cycles for YH_xO_y and GdH_xO_y is shown in Figs. 4(a) and 4(b) and Figs. 4(c) and 4(d), respectively. The corresponding changes in the wing parameter W are shown in Appendix C. The results show that the S parameter increases upon illumination and it decreases partially reversibly during bleaching for both the YH_xO_y and GdH_xO_y films, consistent with our previous DB-PAS study [10]. During the first three cycles, in addition to the reversible part of the shifts in S parameter with photodarkening and bleaching, the S parameter after each photodarkening-bleaching cycle increases successively. The nature of this irreversible increase in the S parameter is discussed in more detail further on.

For the second three cycles, the increase in S parameter under illumination is nearly fully reversed after bleaching. The S-W diagrams presented in Fig. 5 show that the corresponding (S,W) values shift back and forth between the (S,W) value for the photodarkened state and the (S,W) value for the bleached state with a lower S and higher W parameter. These reversible shifts of the positron Doppler broadening S and W parameters occur systematically for each of the second three cycles for all oxyhydride films, and correlate with the reversible changes in the transmittance upon photodarkening and bleaching. As discussed in our previous study, the reversible changes in the Doppler parameters and in the optical transmittance during photodarkening and bleaching can be explained by reversible formation and disappearance of metallic-like nanodomains in the semiconducting oxyhydride matrix [10]. Indeed, the reversible shifts of the Doppler parameters to a larger S parameter and a smaller W parameter point in the direction of the (S,W) value of the rare-earth dihydride [10], in line with the reversible formation of metallic-like nanodomains. In Ref. [10], two types of mechanisms for the formation of metallic-like domains were proposed, which both involve liberation of hydrogen atoms from their lattice positions by the illumination, namely (i) the formation of hydrogen-rich domains enabled by local transport of hydrogen and oxygen ions, which might acquire a metallic-like character due to a mixed Y^{2+}/Y^{3+} valence state (e.g., YH_2O_x with $x < 0.5$), and (ii) the occurrence of an Anderson-Mott insulator-to-metal transition in domains of the film, induced by the formation of a sufficiently high local concentration (above ~30%) of hydrogen vacancies at the octahedral sites and subsequent band formation of photoexcited electrons that occupy Y(4d) orbitals surrounding the hydrogen vacancies [10].

In addition to the reversible shifts of the S parameter, Fig. 4 clearly shows that the S parameter after each photodarkening-bleaching cycle (blue symbols) increases successively for the first three cycles for all samples. Quantitatively, the S parameter after these photodarkening-bleaching cycles has increased by ~3 and 5–6% for YH_xO_y and GdH_xO_y, respectively, compared to the initial S parameter before the first illumination.

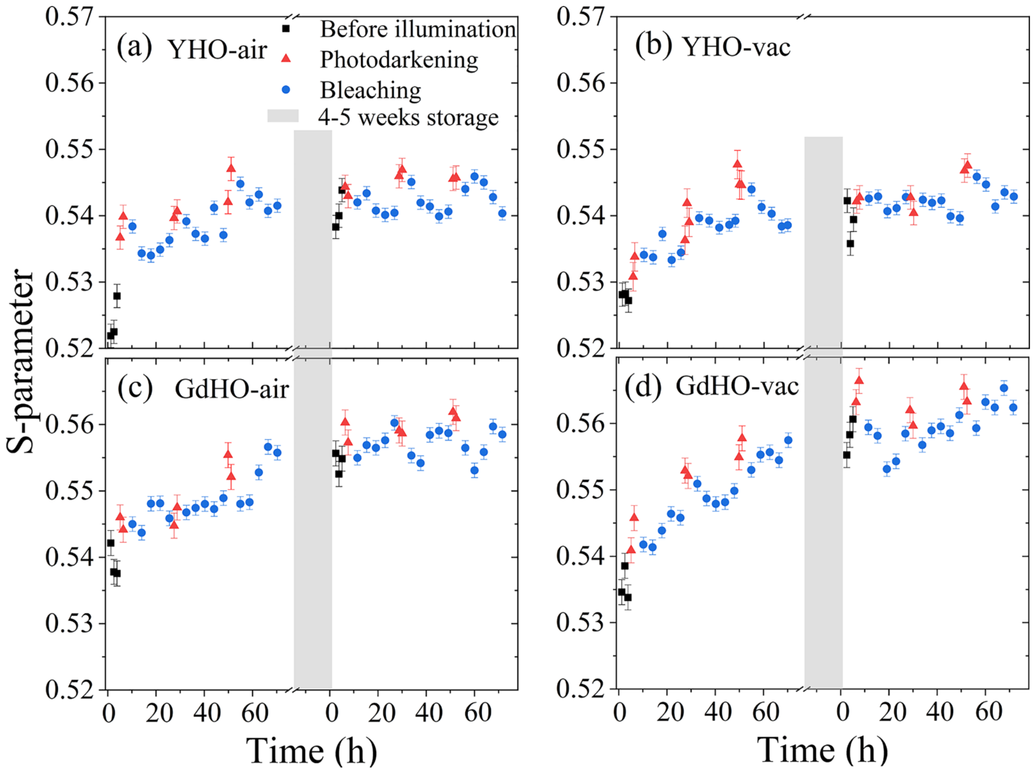

FIG. 4. Time evolution of the S parameter at a positron implantation energy of 5.5 keV for samples (a) YHO-air and (b) YHO-vac, and at a positron implantation energy of 10 keV for samples (c) GdHO-air, and (d) GdHO-vac before illumination (black points) and under six photodarkening (red points)-bleaching (blue points) cycles, including an intermediate storage period of 4–5 weeks (gray region).

These increments are similar to the changes extracted from VEPFIT analysis of the DB-PAS depth profiles before and after the first three cycles as described in details in Appendix D. Simultaneously, the W parameter shows a decrease by ~4 and ~7% for the YH_xO_y and GdH_xO_y samples, respectively. After 4–5 weeks of storage, the S parameter is still high, suggesting that the microstructural changes induced in the photodarkening-bleaching cycles are stable. During the second set of three photodarkening-bleaching cycles, the S parameter after bleaching remains nearly constant with subsequent cycles for each oxyhydride film. This saturation of the S parameter after bleaching could be due to either (i) the concentration and size of open-volume defects do not noticeably increase anymore with the photodarkening-bleaching cycling, or (ii) the concentration of vacancy defects still increases but exceeds the sensitivity of DB-PAS due to saturation trapping of positrons in these defects that will occur when concentrations of order $\sim 10^{-4}$ or higher are reached [12,22].

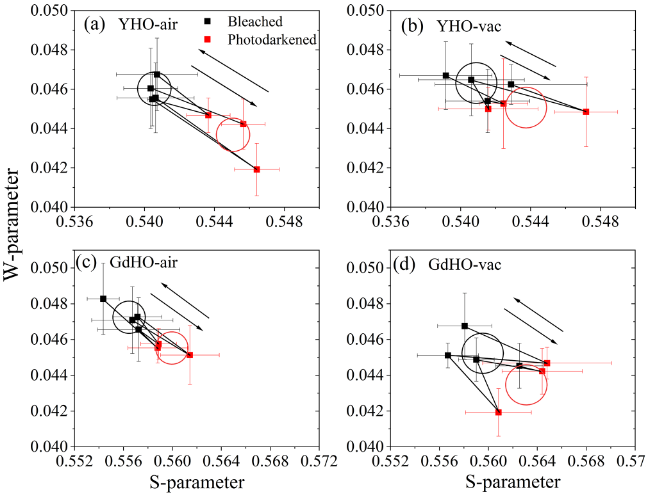

FIG. 5. S,W plots of the second three photodarkening-bleaching cycles for the bleached state (black points) and photodarkened state (red points) for (a) YHO-air, (b) YHO-vac, (c) GdHO-air, and (d) GdHO-vac. The circles and arrows are a guide for the eyes. The center of each circle is located at the average value of each bleached and photodarkening state.

These trends in the S and W parameters upon photochromic cycling are further illustrated in the corresponding S-W diagrams of Figs. 6(a) and 6(b) and Figs. 6(c) and 6(d) for the Y-based and Gd-based oxyhydride films, which reveal the systematic increase in S parameter and decrease in W parameter in the bleached states upon photochromic cycling, together with a comparison to the (S,W) values of the respective yttrium and gadolinium rare-earth metal, metal hydride and oxide films determined in our previous studies [2,10]. It is found that upon photochromic cycling for the first three cycles, the (S,W) values after bleaching for each cycle progressively shift in the same direction towards higher S and lower W, with a slope that is smaller than the line connecting the (S,W) values of the rare-earth metal oxyhydride and rare-earth metal hydride films. These observed linear shifts of the (S,W) values are in line with either a systematic increase in the concentration of

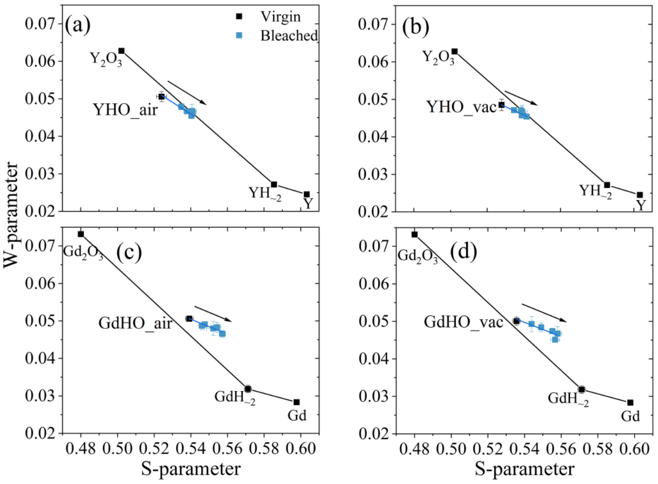

FIG. 6. (S,W) values of (a), (b) Y-based and (c), (d) Gd-based oxyhydride films in the virgin state and in the bleached state upon cycling extracted from the *in situ* illumination DB-PAS measurements, compared with the (S,W) values of the Y-based or Gd-based metal, metal hydride, and oxide films [10]. The arrows are a guide for the eyes, showing the trends for the six cycles.

open-volume defects formed during photochromic cycling or a progressive systematic increase in the size of the vacancy defects.

C. Correlation between photochromic responses and microstructural changes

The previous sections showed a systematic increase in the positron Doppler-broadening S parameter after bleaching as well as in the timescale of bleaching, τ_{bleach}, with photodarkening-bleaching cycling. This suggests that the microstructural changes corresponding to the changes in S parameter may correlate with the memory effect. In order to examine this correlation, the averaged S parameter after each photodarkening-bleaching cycle is plotted in Fig. 7 versus τ_{bleach} for each cycle. For the first three cycles, S parameter rises almost linearly with increasing bleaching time, τ_{bleach}. This strong correlation suggests that the progressively slower bleaching kinetics upon cycling is accompanied by an increased concentration or size of open-volume defects. Our study thus clearly points to a relationship between bleaching kinetics (τ_{bleach}) and formed vacancy structure. After the third illumination and bleaching cycle, the S parameter stays nearly constant. This could be due to the formation of a stable composition of vacancies, or to positron saturation trapping at open-volume defects, meaning that additionally formed vacancies do not induce an observable change in S parameter. After the fourth photodarkening-bleaching cycle, the bleaching time τ_{bleach} also remains constant.

D. Nature of the vacancy-related defects induced by cycling investigated by PALS

To gain more insights into the origin of the irreversible systematic increase in S parameter and decrease in W parameter observed upon photodarkening-bleaching cycling, two YH_xO_y films were measured in the virgin state and in the bleached state after one photodarkening-bleaching cycle by *in situ* PALS at HZDR. All positron lifetime spectra were decomposed by a three-component analysis, shown in Fig. 8.

The extracted lifetimes and the corresponding intensities are shown in Table II. The first and second positron lifetimes in both films are larger than the reported bulk lifetime (∼240 ps) extracted from a two-defect trapping model in our previous study [10]. The reported bulk lifetime is close to the theoretical bulk lifetimes of ∼231 and ∼241 ps in $YH_{2.5}O_{0.25}$ calculated using the two-component density-functional theory (DFT) within the local density approximation (LDA) and generalized gradient approximation (GGA) framework, respectively. More details on the methods employed in the DFT calculation can be found in Appendix E. The reason for using the composition $YH_{2.5}O_{0.25}$ for the theoretical positron lifetime calculation is that a recent DFT study showed that $YH_{2.5}O_{0.25}$ and YHO have a lower total energy compared to the intermediate compositions, and therefore $YH_{2.5}O_{0.25}$ could be the main component of our hydrogen-rich oxyhydride films [23]. The large lifetimes and the intensities of the

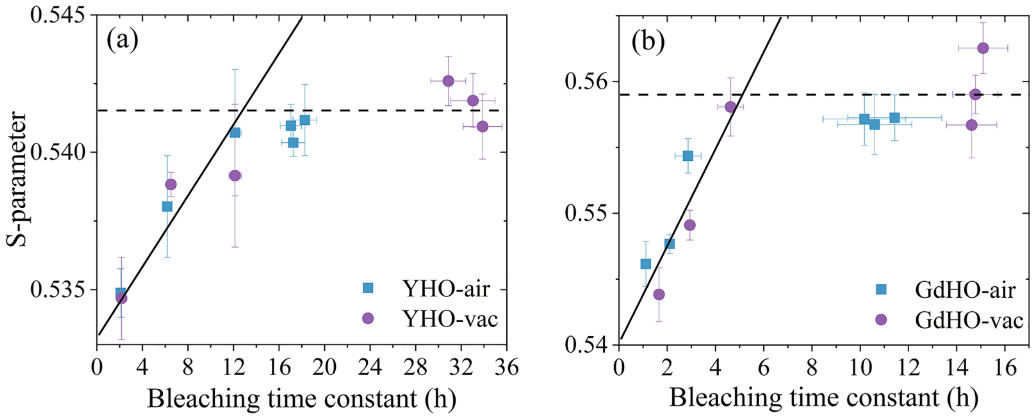

FIG. 7. The averaged S parameter after bleaching versus the bleaching-time constant τ_{bleach}, according to the time-dependent DB-PAS measurements and the optical transmittance measurements for YHO-air, YHO-vac, GdHO-air, and GdHO-vac samples. The solid tilted lines are a guide for the eyes for the first three cycles (suggesting a linear correlation for the first three cycles) and the dashed horizontal lines are a guide for the eyes for the second three cycles.

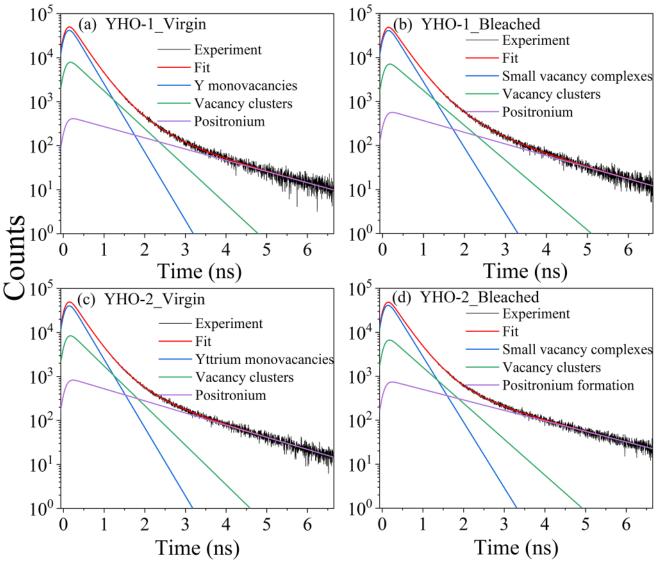

FIG. 8. Positron lifetime spectra collected at an implantation energy of 5 keV of (a) YHO-1 in the virgin state and (b) the bleached state after one cycle, and (c) YHO-2 in the virgin state and (d) the bleached state after one cycle, and the corresponding three-component analyses. The background was less than 1 for all fits.

experimental first and second positron lifetime components together with the absence of a (reduced) bulk lifetime component indicate positron saturation trapping for these samples due to a high vacancy concentration of the order of 10^{-4} or higher, i.e., almost all (>99%) implanted positrons are trapped and annihilate at vacancy-type defects. In the virgin state of both films, the first lifetime component with τ_1 of ~280 ps is close to the calculated values ~290 ps (LDA) and ~324 ps (GGA) for yttrium monovacancies; therefore, this component could be assigned to yttrium monovacancies (V_Y) present in the as-deposited films. We note here that we cannot strictly exclude the possibility of hydrogen-decorated metal vacancies, as have been observed in the niobium, nickel, and tungsten systems [24–27]. These studies showed that the decoration of a metal vacancy with one hydrogen atom can decrease the positron lifetime at a cation monovacancy by 10–20 ps. However, yttrium oxyhydride is different from the above-mentioned transition metals in the sense of its mostly ionic binding of the metal cation (Y^{3+}) and the hydrogen (H^-) and oxygen (O^{2-}) anions, leading to a high stability of the formed oxyhydride phase [28]. For yttrium oxyhydride films, it is likely that during the reactive magnetron sputtering process and subsequent postoxidation, hydrogen atoms strongly prefer anion (tetrahedral and octahedral) lattice sites of the stable oxyhydride phase, rather than vacant cation lattice sites (cation monovacancies). Similarly, no hydrogen-decorated small vacancies were found in hydrogenated MgTi-based ionic compounds [29]. The relatively high intensity I_1 (~73–76%) indicates that these vacancies are dominant positron trapping sites. The longer lifetime of the second component τ_2 of ~500 ps with an intensity of 21% stems from annihilation in large vacancy clusters (consisting of >5 vacancies [10]), while the third component with the longest lifetime τ_3 in the range of ~1.6–1.7 ns is a characteristic of ortho-positronium (o-Ps) formed in nanoscale open volume (such as nanopores) present in the films. Assuming pores that are spherically shaped, the diameter can be estimated to be around 0.50 nm according to Tao-Eldrup model [30,31]. Both positron annihilation and o-Ps formation might therefore occur in the same type of vacancy clusters [10].

After ~2 h illumination and 2–3 h of bleaching in the dark, both τ_1 and τ_2 have increased in the same manner for both samples, indicating growth of the corresponding vacancies and vacancy clusters. The first lifetime τ_1 increases to ~290 ps, which can be attributed to the formation of divacancies or small multivacancy complexes, involving Y monovacancies present in the as-deposited films and light-induced hydrogen vacancies. Local hydrogen (hopping) mobility has been proposed to be a key element of photochromism in rare-earth oxyhydride films [32–34]. This can be understood, since under the photoexcitation of charge carriers across the band gap, hydrogen ions at octahedral sites may capture photogenerated holes ($H^- + h^+ \rightarrow H^0$) and leave their lattice positions, producing hydrogen-vacant sites in the lattice. Some of these hydrogen vacancies may aggregate with yttrium monovacancies to form divacancies $V_Y{-}V_H$, or perhaps even small vacancy complexes consisting of V_Y and a few hydrogen vacancies. In principle, the formation of $V_Y{-}V_O$ is also possible, although O is considered to be less mobile than H due to its lower polarity and larger mass, and liberation from its lattice position is less probable [28,35]. Notably, the increase in τ_1 after bleaching is ~4%, and therefore clearly smaller than the typical increase in lifetimes (>10%) going from monovacancies to divacancies in semiconductors such as Si, GaAs, and SiC [36,37]. This suggests that only part of the yttrium monovacancies turn into divacancy-like defects, meaning that a mixture of monovacancies and divacancy-like defects is present in the films after one photodarkening-bleaching cycle. Such a transformation from monovacancies to divacancy-like defects for only part of the Y monovacancies present is understandable. If we assume that the mobility of hydrogen vacancies is small, V_Y and V_H can only aggregate when a hydrogen vacancy is created on a lattice site adjacent

TABLE II. Time-averaged positron lifetimes (τ_i) and intensities (I_i) for two YH_xO_y films in the virgin state and in the bleached state after one photodarkening-bleaching cycle, extracted from PALS spectra collected at 5 keV.

Sample	Status	τ_1 (ps)	τ_2 (ps)	τ_3 (ns)	I_1 (%)	I_2 (%)	I_3 (%)
YHO-1	Virgin state	279 ± 2	506 ± 12	1.71 ± 0.03	76 ± 2	21 ± 1	2.9 ± 0.1
	Bleached state after one cycle	290 ± 2	546 ± 15	1.66 ± 0.03	76 ± 1	21 ± 1	3.8 ± 0.2
YHO-2	Virgin state	280 ± 2	484 ± 16	1.57 ± 0.02	73 ± 2	21 ± 2	5.4 ± 0.1
	Bleached state after one cycle	291 ± 2	532 ± 18	1.81 ± 0.03	76 ± 2	18 ± 2	5.5 ± 0.1

to the yttrium vacancy. Considering now the concentration of hydrogen vacancies at octahedral sites that are formed during the first photodarkening (we assume an average concentration of octahedral hydrogen vacancies of the order of ∼10% of all octahedral hydrogen in the film, which would be a reasonable value in the framework of the Anderson-Mott model) and the concentration of preexisting yttrium vacancies V_Y (of the order of 10^{-4}) [10], one can estimate that the probability of formation of a hydrogen vacancy adjacent to an Y monovacancy is on the order of ∼25% [38]. Therefore, we can expect a concentration of formed divacancy-like defects of the order of 10^{-5}, i.e., somewhat smaller than the concentration of V_Y and likely below the concentration threshold for saturation trapping of positrons. The increase in the lifetime of the second component τ_2 of 40–50 ps after one cycle is rather large, and could be due to the release of loosely bonded hydrogen atoms from the walls of the large vacancy clusters or of dihydrogen molecules from these vacancy clusters [7]. The change in the third component varies from sample to sample. Overall, the increase in *S* parameter after one photodarkening-bleaching cycle could be the result of the clustering of hydrogen vacancies (created by the illumination) with the preexisting Y monovacancies, forming divacancies (or small vacancy complexes), and of hydrogen liberated from vacancy clusters, as inferred from the PALS study, in combination with incomplete refilling of hydrogen vacancies during the bleaching process. Alternatively, a small amount of nanoscale metallic-like domains that possibly remain present after bleaching may also lead to an irreversible increase in the *S* parameter. This process cannot be completely ruled out from the PALS measurements of this study, since the lifetime of positrons that trap and annihilate in the metallic-like domains and the exact nature of the metallic-like domains is yet unknown. However, we note here that the reported positron bulk lifetime of metallic yttrium dihydride of ∼260 ps [10] is smaller than that of the lifetime of the first component of the yttrium oxyhydride samples both in the as-deposited state (∼280 ps) and after a full photodarkening-bleaching cycle (∼290 ps, i.e., *increased* by ∼10 ps), making this alternative explanation less probable.

Finally, we note here that since the PALS measurements after one photodarkening-bleaching cycle suggest that only part of the initially present Y monovacancies transform into divacancy-like defects, it is likely that more divacancy-like defects will be formed in the subsequent cycles. Clearly, this may explain the systematic increase in *S* parameter in the bleached state observed during the first three photochromic cycles.

IV. DISCUSSION

Our studies show that both yttrium and gadolinium oxyhydride thin films exhibit a reversible photochromic effect upon six consecutive photodarkening-bleaching cycles, in which the transmittance is able to recover back to its original state after bleaching. However, the bleaching kinetics becomes increasingly slower upon cycling for the first four cycles, after which the bleaching rate stabilizes. Interestingly, our studies reveal a clear correlation between the progressively larger bleaching-time constants and the evolution of the positron Doppler *S* parameter as detected after each photodarkening-bleaching cycle. In combination with the PALS results, this suggests that the slower bleaching process upon cycling is accompanied by an increased concentration of divacancy-like defects and growth of vacancy clusters due to hydrogen liberated from their (lattice) positions. In order to gain further understanding of the memory effect from such a microscopic perspective, we propose and discuss a number of possibilities in the context of this positron study.

A. Increase in diffusion time

The slow bleaching kinetics of the order of hours for both yttrium and gadolinium oxyhydride films, as depicted in Fig. 2, could be caused by diffusion of hydrogen anions acting as a rate-limiting process for the return of the film to the transparent state. This hypothesis of hydrogen diffusion can be evaluated in the context of proposed mechanisms for the photochromism that involve the formation of metallic domains, such as (i) phase-segregated hydrogen-rich domains enabled by local transport of hydrogen and oxygen ions liberated during illumination, which might acquire a metallic-like character due to a mixed Y^{2+}/Y^{3+} valence state (e.g., YH_2O_x with $x < 0.5$), in a hydrogen-poor transparent matrix, and (ii) Anderson-Mott transition in certain domains of the yttrium oxyhydride films where the concentration of illumination-induced hydrogen vacancies and subsequently nearby trapped electrons localized in $Y(4d)$ orbitals is sufficiently high to lead to electron band formation and local metallicity [10,32,39]. Indeed, high hydrogen anion conduction is observed in powder La and Nd oxyhydrides, albeit other rare-earth oxyhydrides show substantially lower macroscopic hydrogen diffusion [40,41].

For a diffusion process, the diffusion time τ_{diff} is proportional to the square of the diffusion distance *L* and is inversely proportional to the diffusion coefficient *D*, according to $\tau_{\text{diff}} \sim \frac{L^2}{D}$ [42]. Therefore an increase in the diffusion distance *L* can lead to an increase in the diffusion time. For example, if hydrogen-rich metallic domains become systematically larger upon cycling during photodarkening, the diffusion distance for hydrogen anions to travel out of the domains will become larger, leading to a longer diffusion time and thus, slower bleaching kinetics. Second, the diffusion coefficient *D* can be influenced by multiple factors, for instance, vacancy defects [43,44]. The increase in concentration of vacancy defects in oxyhydride films upon cycling, as observed in this study, may provide more hydrogen anion trapping sites, resulting in a smaller diffusion coefficient and a longer diffusion time. Such trapping of hydrogen in vacancies was observed in for example monoclinic zirconia, which decreased the diffusion coefficient and slowed down the hydrogen diffusion [43].

B. Loss of hydrogen

Another possible cause for the gradual slowdown of bleaching kinetics upon cycling could be the loss of hydrogen, since the local hydrogen composition is expected to be important in regaining transparency. Previous studies into the nature of the photochromism provided indications that hydrogen is a key element in the photochromic effect in rare-earth oxyhydride films [10,32,39].

Within the Anderson-Mott insulator-to-metal transition proposed in Ref. [10] and briefly discussed here in Sec. III B, the bleaching process requires the refilling with hydrogen of a sufficient amount of hydrogen vacancies in order to reduce the concentration of trapped electrons near such hydrogen vacancies to below the threshold concentration for metallicity in a domain and reach the original semiconductor (transparent) state. However, hydrogen may get lost due to trapping at (for example) grain boundaries, or/and due to outdiffusion of hydrogen to the environment. Indeed, Moldarev *et al.* [7] observed hydrogen effusion in yttrium oxyhydride films for the first and second photodarkening-bleaching cycles. The loss of hydrogen will reduce the amount of mobile hydrogen with respect to the amount of hydrogen liberated from lattice positions in the film during photodarkening. This may result in a slower bleaching kinetics, since some of the hydrogen required to refill the hydrogen vacancies in the metallic areas will need to come from a larger distance.

Indeed, the case of hydrogen loss seems to be in line with the irreversible formation of divacancies observed in our positron annihilation study, since hydrogen atoms that leave their lattice positions during photodarkening and are lost from the film will cause irreversible creation of hydrogen vacancies. Some of these hydrogen vacancies may aggregate with the preexisting yttrium monovacancies, explaining the increase in the lifetime of the first component τ_1 and the increase in the S parameter after bleaching. Also, hydrogen removal from the larger vacancy clusters will lead to growth in the open volume of these clusters, in line with the observed increase in τ_2. Furthermore, the progressive increase in the S parameter after bleaching upon cycling can be naturally explained when the hydrogen loss occurs primarily in the first three cycles, in line with the observations by Molderav *et al.* [7].

C. Grain growth

Komatsu *et al.* demonstrated that epitaxially grown yttrium oxyhydride films exhibit an extremely slow bleaching rate, as the high conductivity of the photoinduced metallic state hardly changes during the ∼50-h-long observation time after the UV illumination had stopped [33]. Hence, the systematic reduction in bleaching kinetics of the yttrium oxyhydride films studied here might be ascribed to a gradual structural transformation from the polycrystalline state in the direction towards epitaxially grown films, which may have larger grain sizes and less grain interfaces [45,46].

However, in both our yttrium and gadolinium oxyhydride samples, the speculation of grain growth is not supported by the *ex situ* XRD results, as the grain size estimated from the peak width of the strongest diffraction peak at $\sim 33^\circ$ using the Scherrer equation does not change within error bars after illumination of ∼2.5 h for both samples (see Appendix F for details on XRD data and analysis).

D. Formation of hydroxide (OH^-)

A mechanism for the photochromic effect in yttrium oxyhydride films that does not rely on diffusion was proposed in Refs. [32,33]. This mechanism involves the local formation of OH^- hydroxyl groups, as has been previously observed in mayenite [47–49]. In this scenario, large polarons are created in the yttrium oxyhydride structure due to the release of electrons according to the local reaction $O^{2-} + H^- + h\nu \rightarrow OH^- + 2e^-$ during illumination [33]. When the concentration of such polarons is large enough, meaning an average distance between polarons below about 7 Å, the localized electron orbitals overlap and form delocalized electron bands. The threshold fraction of formed OH^- hydroxide bonds to induce metallic conductivity within this polaron mechanism was estimated to be $\sim 2.2\%$ according to percolation theory [33]. Indeed, the formation of such a concentration of metallic areas under illumination can be observed by positrons [10] and is consistent with the observed increase in S parameter during illumination (Fig. 4). However, in Ref. [33] it was reported that the transparent state could only be recovered when annealing the photodarkened sample to a high temperature of 125 °C, which would point to a high activation barrier for the reverse reaction $OH^- + 2e^- \rightarrow O^{2-} + H^-$ [33]. This suggests that if such local polaron formation is the sole actor in the mechanism in photodarkening and bleaching process, it is hard to explain the much faster bleaching observed in our oxyhydride films.

V. CONCLUSIONS

A stable cycling performance is of great importance for applications of photochromic YH_xO_y and GdH_xO_y thin films. We investigated the optical responses of photochromic YH_xO_y and GdH_xO_y thin films under six photodarkening-bleaching cycles by *in situ* illumination transmittance measurements. In both systems, the transmittance recovers after each photodarkening-bleaching cycle, while a slowing down of the bleaching kinetics is observed upon cycling (the memory effect). The microstructural evolution in both YH_xO_y and GdH_xO_y films under the same six photodarkening-bleaching cycles is investigated by *in situ* illumination DB-PAS and by PALS after one cycle. For the first three cycles, DB-PAS shows a systematic increase in the S parameter after bleaching upon cycling, and a strong correlation between the S parameter and the bleaching-time constant is observed. This correlation suggests that the microstructural changes corresponding to the slower bleaching upon cycling involve vacancy aggregation, supported by PALS studies that show the formation of divacancies and growth of vacancy clusters. The change in the open-volume defects may affect the diffusion time by reducing the diffusion coefficient, supposing bleaching is a diffusion-related process. Moreover, hydrogen vacancies that cannot be refilled due to hydrogen loss may also contribute to a slower bleaching kinetics. For the second three cycles, the reversible shifts in the Doppler parameters back and forth between the photodarkened state and the bleached state could be due to the reversible formation of metallic-like domains, pointing to previously proposed mechanisms of the photochromism.

ACKNOWLEDGMENTS

The authors thank Martijn de Boer, Robert Dankelman, and Michel Steenvoorden for their technical assistance. This research was financially supported by Guangzhou Elite Project and the Materials for Sustainability programme (Grant No. 680.M4SF.034) of the Dutch Research Council. Parts of this research were carried out at ELBE at the Helmholtz-Zentrum Dresden - Rossendorf e. V., a member of the Helmholtz Association, and we would like to thank the facility staff for assistance.

APPENDIX A: POSITRON FRACTIONS AS A FUNCTION OF IMPLANTATION ENERGY FOR YTTRIUM AND GADOLINIUM OXYHYDRIDE FILMS FIG. 9

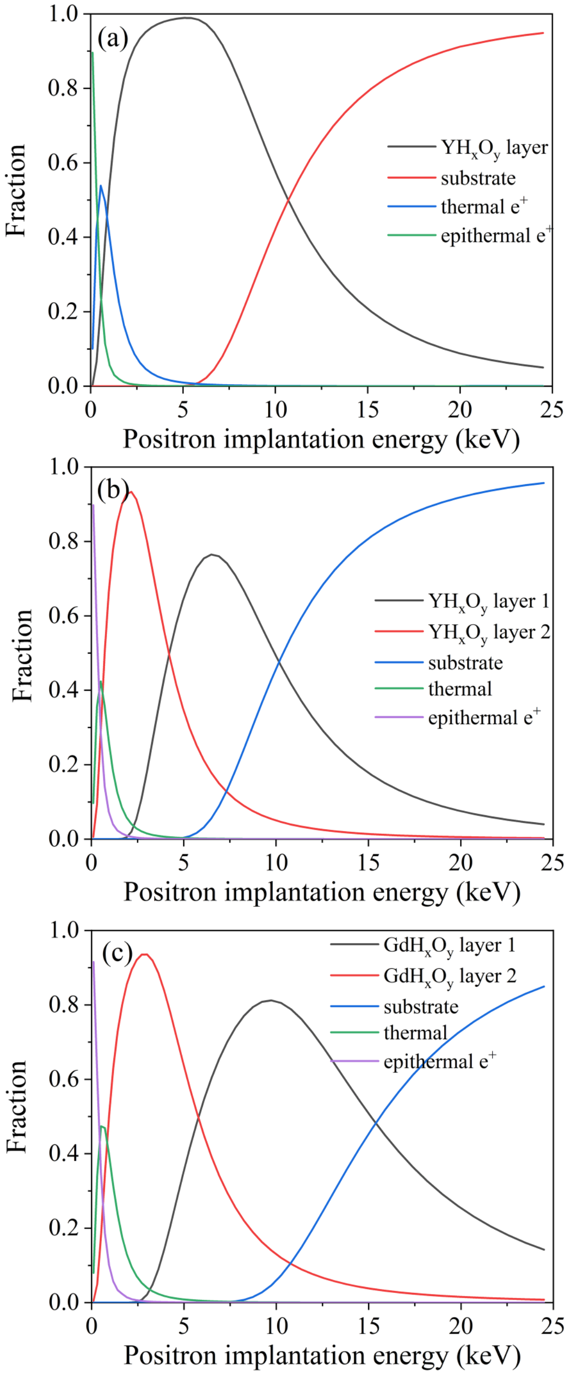

FIG. 9. The fractions of positrons annihilating in each layer in the YH_xO_y and GdH_xO_y films as a function of positron implantation energy derived by VEPFIT analysis, using a (a) one-layer or (b) two-layer model for the YH_xO_y layer, and (c) a two-layer model for the GdH_xO_y layer.

APPENDIX B: DERIVATION OF THE BLEACHING-TIME CONSTANT FIG. 10

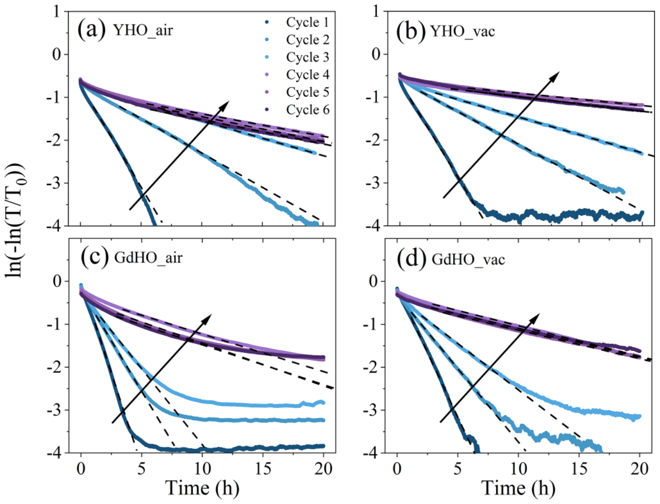

FIG. 10. The natural logarithm of the negative natural logarithm of the normalized optical transmittance as a function of bleaching time, and corresponding linear best fits (dashed lines) used to derive the bleaching-time constant according to Eq. (2).

APPENDIX C: TIME EVOLUTION OF THE *W* PARAMETER UPON PHOTODARKENING-BLEACHING CYCLING FIG. 11

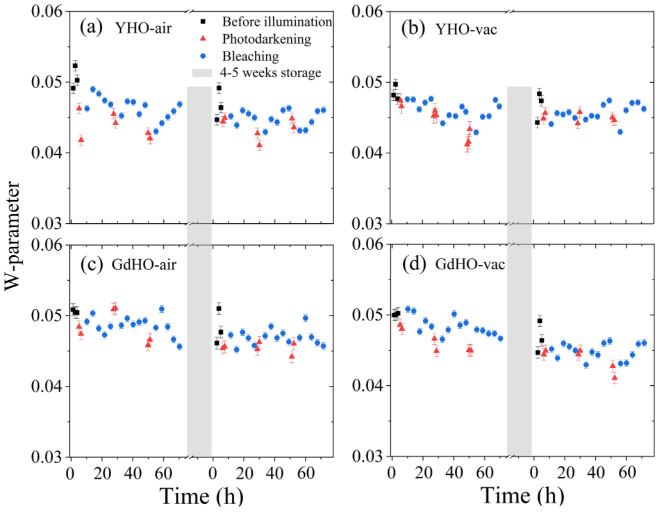

FIG. 11. Time evolution of *W* parameter at a positron implantation energy of 5.5 keV for (a) YHO-air and (b) YHO-vac, and at a positron implantation energy of 10 keV for (c) GdHO-air and (d) GdHO-vac under six photodarkening(red)-bleaching(blue) cycles, including an intermediate storage period of 4–5 weeks under ambient or vacuum conditions (gray region).

APPENDIX D: DB-PAS DEPTH PROFILES AND VEPFIT ANALYSES

TABLE III. The best-fit parameters of DB-PAS depth profiles for the oxyhydride layer of YHO-air in the virgin state, after the first three cycles, before the second three cycles, and after the second three cycles.

		Near-surface oxyhydride layer			Bulk oxyhydride layer			
Sample	State	*d*1 (nm)	*S*1	*W*1	*d*2 (nm)	*S*2	*W*2	L_{d2} (nm)
YHO-air	Virgin state	60 (5)	0.529 (1)	0.0504 (3)	360	0.525 (1)	0.0478 (5)	60 (3)
	After the first three cycles				360	0.542 (1)	0.0458 (3)	30 (2)
	Before the second three cycles				300	0.544 (1)	0.0431 (3)	30 (3)
	After the second three cycles				360	0.541 (1)	0.0468 (3)	15 (1)

TABLE IV. The best-fit parameters of DB-PAS depth profiles for the oxyhydride layer of YHO-vac in the virgin state, after the first three cycles, before the second three cycles, and after the second three cycles.

Sample	State	*d* (nm)	*S*	*W*	L_d (nm)
YHO-vac	Virgin state	360	0.526 (1)	0.0480 (5)	30 (2)
	After the first three cycles	360	0.541 (1)	0.0461 (3)	10 (1)
	Before the second three cycles	360	0.537 (1)	0.0475 (2)	37 (3)
	After the second three cycles	360	0.542 (1)	0.0484 (3)	30 (1)

TABLE V. The best-fit parameters of DB-PAS depth profiles for the oxyhydride layer of GdHO-air in the virgin state, after the first three cycles, before the second three cycles, and after the second three cycles.

		Near-surface oxyhydride layer			Bulk oxyhydride layer			
Sample	State	*d*1 (nm)	*S*1	*W*1	*d*2 (nm)	*S*2	*W*2	L_{d2} (nm)
GdHO-air	Virgin state	60	0.522 (1)	0.0551 (3)	360	0.545 (1)	0.0460 (5)	70 (3)
	After the first three cycles	60	0.538 (1)	0.0505 (3)	360	0.565 (1)	0.0433 (3)	45 (2)
	Before the second three cycles	60	0.534 (1)	0.0503 (3)	360	0.564 (1)	0.0436 (3)	30 (2)
	After the second three cycles	60	0.540 (1)	0.0502 (3)	360	0.567 (1)	0.0451 (3)	30 (2)

TABLE VI. The best-fit parameters of DB-PAS depth profiles for the oxyhydride layer of GdHO-vac in the virgin state, after the first three cycles, before the second three cycles, and after the second three cycles.

		Near-surface oxyhydride layer			Bulk oxyhydride layer			
Sample	State	*d*1 (nm)	*S*1	*W*1	*d*2 (nm)	*S*2	*W*2	L_{d2} (nm)
GdHO-vac	Virgin state	60	0.525 (1)	0.0533 (3)	360	0.534 (1)	0.0486 (3)	60 (5)
	After the first three cycles	60	0.539 (1)	0.0489 (3)	360	0.565 (1)	0.0454 (3)	48 (2)
	Before the second three cycles	60	0.542 (1)	0.0504 (3)	360	0.563 (1)	0.0447 (3)	48 (2)
	After the second three cycles	60	0.542 (1)	0.0506 (3)	360	0.571 (1)	0.0441 (3)	33 (2)

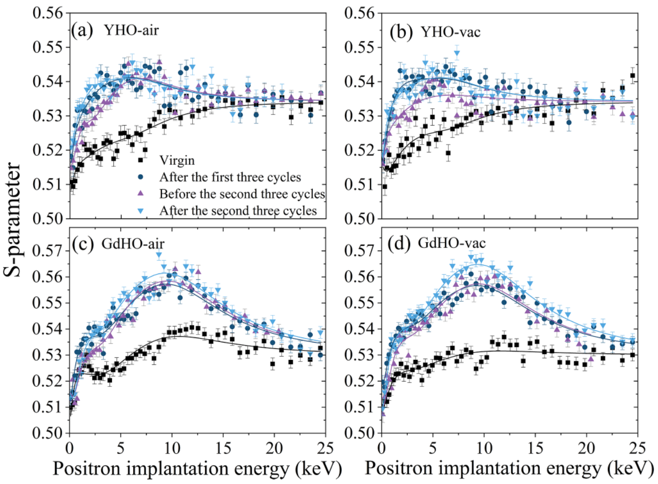

FIG. 12. DB-PAS depth profiles of (a) YHO-air, (b) YHO-vac, (c) GdHO-air, and (d) GdHO-vac in the virgin state (black color), after the first three photodarkening-bleaching cycles (dark blue color), before the second three cycles (purple color), and after the second three cycles (light-blue color).

Figure 12 shows the DB-PAS *S*-parameter depth profiles for all four samples: (a) YHO-air, (b) YHO-vac, (c) GdHO-air, and (d) GdHO-vac in the virgin state, after the first three cycles, before the second three cycles, and after the second three cycles. In order to minimize the number of fit parameters, the *S* parameter and *W* parameter of the fused-SiO_2 substrate layer were fixed to 0.5325 and 0.059, as extracted from the high implantation energy range (20–25 keV). The density and diffusion length (L_d) of the fused-SiO_2 substrate layer were fixed to 2.2 g/cm^3 and 25 nm. According to VEPFIT analysis of the depth profiles after the first three cycles, the thickness (d) of the oxyhydride layer of the YH_xO_y samples is 360 nm, so the layer thicknesses were fixed at this value for the depth profiles collected at the other stages of cycling. For the YHO-air sample before the second three cycles, the *S* parameter of the bulk oxyhydride layer (at 5 keV) seems to be unchanged, while the *S* parameter of the oxyhydride layer near the surface region decreases, so an additional near-surface layer was added to the model. The thicknesses of the near-surface oxyhydride oxyhydride layer and bulk oxyhydride layer are noted as $d1$ and $d2$, respectively. For the GdH_xO_y samples, in addition to the bulk oxyhydride layer (at 10 keV), an additional much thinner oxyhydride layer near the surface region below 5 keV for each depth profile is seen; therefore, a two-layer model for the gadolinium oxyhydride layer is utilized. According to VEPFIT analysis of the depth profile after the first three cycles, the thickness of the near-surface and bulk oxyhydride layer of the GdH_xO_y samples are 60 and 360 nm, respectively, so the total thickness is 420 nm. The layer thicknesses were fixed at these values for the rest of the depth profiles of GdH_xO_y samples, assuming the thickness of the near-surface layer remains the same at other stages of cycling. A density of 4.3 and 7.2 g/cm^3 was used for the YH_xO_y and GdH_xO_y oxyhydride layers, respectively. A two- or three-layer model (including one layer for the semi-infinite substrate layer) was used in the VEPFIT analysis. The corresponding results of the best-fit analysis are shown in Tables III–VI.

When assuming a (reasonable) value for the positron diffusion coefficient D_+ of $\sim$1 cm^2/s at room temperature [11,12], and taking into account the bulk positron lifetime of $\tau_{\text{bulk}} \sim$ 240 ps in the YH_xO_y films [10], the bulk positron diffusion length L_{bulk} in defect-free YH_xO_y can be estimated, according to $L_{\text{bulk}}=\sqrt{D_+\tau_{\text{bulk}}}=\sqrt{1\times 240\times 10^{-12}}\times 10^7$ nm $\approx$ 150 nm [22]. If the vacancy concentration C_d is near the upper limit of saturated trapping, e.g., on the order of 10^{-4} [10,12,22], the effective positron diffusion length L_+ can be estimated to be around 30 nm, according to $k_d=\mu C_d = D_+(\frac{1}{L_+^{\,2}}-\frac{1}{L_{\text{bulk}}^{\,2}})$, assuming the positron trapping coefficient μ is 1×10^{15} s^{-1} [11,22].

APPENDIX E: POSITRON LIFETIME CALCULATION METHODS

We employed the self-consistent two-component density-functional theory calculations in the open-source ABINIT package to calculate the positron bulk lifetime and the positron lifetime of yttrium monovacancies in $YH_{2.5}O_{0.25}$ [50,51]. The positron lifetimes of yttrium vacancies were calculated after complete lattice relaxation. Calculations were performed with the $Fm\bar{3}m$ structure of $YH_{2.5}O_{0.25}$ using a $2\times 2\times 2$ supercell containing 120 atoms. The atomic configurations were produced using the ATOMPAW code [52]. The ground states of electrons and the positron were calculated by the projector augmented-wave method. The exchange-correlation interactions were described by the local density approximation (LDA) and the generalized gradient approximation (GGA). For LDA, we employed the Teter-Pade parametrization [53] and the zero-positron density limit of Arponen and Pajanne, as implemented by Boronski and Nieminen [54]. For the GGA calculations, the Perdew-Burke-Ernzerhof functional [55] was combined with the same exchange-correlation functionals as we used for LDA, supplemented by correction terms provided by Barbiellini *et al.* [51]. All positron lifetimes were calculated using the enhancement factor given by Boronski and Nieminen in the random-phase approximation limit [54].

APPENDIX F: X-RAY DIFFRACTION FIG. 13

The average size of grains was estimated from the peak width of an x-ray-diffraction peak using Scherrer's equation $d_{\text{grain}}=\frac{k\lambda}{\beta_{\text{sample}}\cos\theta}$ and $\beta_{\text{sample}}=\sqrt{\beta_{\text{total}}^2-\beta_{\text{instrument}}^2}$, where d_{grain}

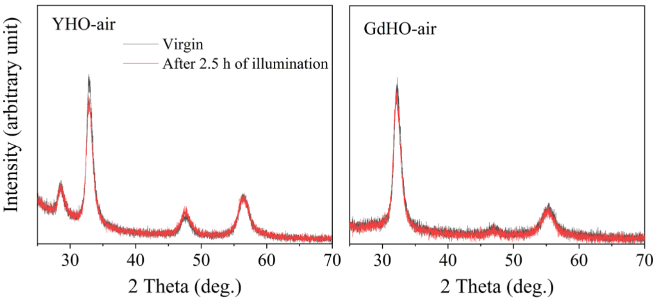

FIG. 13. X-ray-diffraction patterns of the YHO-air and GdHO-air samples before and after illumination for 2.5 h.

is the average grain size in nm, λ is the x-ray wavelength in nm, θ is the diffraction angle, and k is Scherrer's constant. Here, we used 0.94 for a cubic structure, β_{total} is the full width at half maximum (FWHM, in radians) of the diffraction peak at ~33° (200) in our case, and $\beta_{\text{instrument}}$ is extracted from an independent XRD measurement on a single-crystal silicon sample. The average grain size for the YHO-air sample in the virgin state and the state right after 2.5 h illumination is 8 ± 0.5 and 8 ± 0.5 nm, respectively. The average grain size for the GdHO-air sample in the virgin state and the state immediately after 2.5 h illumination is 7 ± 0.5 and 7 ± 0.5 nm, respectively. In this analysis, other factors that may also cause the peak broadening, for instance, strain, are not included.

[1] F. Nafezarefi, H. Schreuders, B. Dam, and S. Cornelius, Photochromism of rare-earth metal-oxy-hydrides, Appl. Phys. Lett. **111**, 103903 (2017).

[2] G. Colombi, T. De Krom, D. Chaykina, S. Cornelius, S. W. H. Eijt, and B. Dam, Influence of cation (RE = Sc, Y, Gd) and O/H anion ratio on the photochromic properties of $\text{REO}_x\text{H}_{3-2x}$ thin films, ACS Photonics **8**, 709 (2021).

[3] C. C. You and S. Z. Karazhanov, Effect of temperature and illumination conditions on the photochromic performance of yttrium oxyhydride thin films, J. Appl. Phys. **128**, 013106 (2020).

[4] F. Nafezarefi, S. Cornelius, J. Nijskens, H. Schreuders, and B. Dam, Effect of the addition of zirconium on the photochromic properties of yttrium oxy-hydride, Sol. Energy Mater. Sol. Cells **200**, 109923 (2019).

[5] D. Chaykina, I. Usman, G. Colombi, H. Schreuders, B. Tyburska-Pueschel, Z. Wu, S. W. H. Eijt, L. J. Bannenberg, G. A. de Wijs, and B. Dam, Aliovalent calcium doping of yttrium oxyhydride thin films and implications for photochromism, J. Phys. Chem. C **126**, 14742 (2022).

[6] T. Mongstad, C. Platzer-Bjorkman, J. P. Maehlen, L. P. A. Mooij, Y. Pivak, B. Dam, E. S. Marstein, B. C. Hauback, and S. Z. Karazhanov, A new thin film photochromic material: Oxygen-containing yttrium hydride, Sol. Energy Mater. Sol. Cells **95**, 3596 (2011).

[7] D. Moldarev, L. Stolz, M. V. Moro, S. M. Adalsteinsson, I. A. Chioar, S. Z. Karazhanov, D. Primetzhofer, and M. Wolff, Environmental dependence of the photochromic effect of oxygen-containing rare-earth metal hydrides, J. Appl. Phys. **129**, 153101 (2021).

[8] M. P. Plokker, S. W. H. Eijt, F. Naziris, H. Schut, F. Nafezarefi, H. Schreuders, S. Cornelius, and B. Dam, Electronic structure and vacancy formation in photochromic yttrium oxy-hydride thin films studied by positron annihilation, Sol. Energy Mater. Sol. Cells **177**, 97 (2018).

[9] S. W. H. Eijt, T. W. H. de Krom, D. Chaykina, H. Schut, G. Colombi, S. Cornelius, W. Egger, M. Dickmann, C. Hugenschmidt, and B. Dam, Photochromic YO_xH_y thin films examined by *in situ* positron annihilation spectroscopy, Acta Phys. Pol. A **137**, 205 (2020).

[10] Z. Wu, T. de Krom, G. Colombi, D. Chaykina, G. van Hattem, H. Schut, M. Dickmann, W. Egger, C. Hugenschmidt, E. Brück, B. Dam, and S. W. H. Eijt, Formation of vacancies and metallic-like domains in photochromic rare-earth oxyhydride thin films studied by *in situ* illumination positron annihilation spectroscopy, Phys. Rev. Mater. **6**, 065201 (2022).

[11] F. Tuomisto and I. Makkonen, Defect identification in semiconductors with positron annihilation: Experiment and theory, Rev. Mod. Phys. **85**, 1583 (2013).

[12] M. J. Puska and R. M. Nieminen, Theory of positrons in solids and on solid surfaces, Rev. Mod. Phys. **66**, 841 (1994).

[13] C. Hugenschmidt, Positrons in surface physics, Surf. Sci. Rep. **71**, 547 (2016).

[14] J. Cizek, Characterization of lattice defects in metallic materials by positron annihilation spectroscopy: A review, J. Mater. Sci. Tech. **34**, 577 (2018).

[15] H. Schut, A Variable Energy Positron Beam Facility with Applications in Materials Science, Ph.D. thesis (Delft University of Technology, Delft, 1990).

[16] A. van Veen, H. Schut, J. Devries, R. A. Hakvoort, and M. R. IJpma, Analysis of positron profiling data by means of VEPFIT, AIP Conf. Proc. **218**, 171 (1990).

[17] V. J. Ghosh, Positron implantation profiles in elemental and multilayer systems, Appl. Surf. Sci. **85**, 187 (1995).

[18] A. Zubiaga, J. A. Garcia, F. Plazaola, F. Tuomisto, J. Zuniga-Perez, and V. Munoz-Sanjose, Positron annihilation spectroscopy for the determination of thickness and defect profile in thin semiconductor layers, Phys. Rev. B **75**, 205305 (2007).

[19] A. Wagner, M. Butterling, M. O. Liedke, K. Potzger, and R. Krause-Rehberg, Positron annihilation lifetime and Doppler broadening spectroscopy at the ELBE facility, AIP Conf. Proc. **1970**, 040003 (2018).

[20] E. Hirschmann, M. Butterling, U. H. Acosta, M. O. Liedke, A. G. Attallah, P. Petring, M. Görler, R. Krause-Rehberg, and A. Wagner, A new system for real-time data acquisition and pulse parameterization for digital positron annihilation lifetime spectrometers with high repetition rates, J. Instrum. **16**, P08001 (2021).

[21] J. V. Olsen, P. Kirkegaard, and M. Eldrup, Analysis of positron lifetime spectra using the PALS*fit*3 program, AIP Conf. Proc. **2182**, 040005 (2019).

[22] R. Krause-Rehberg and H. S. Leipner, *Positron Annihilation in Semiconductors - Defect Studies* (Springer, Berlin, 1999).

[23] S. Banerjee, D. Chaykina, R. Stigter, G. Colombi, S. W. H. Eijt, B. Dam, G. A. de Wijs, and A. P. M. Kentgens, Exploring multi-anion chemistry in yttrium oxyhydrides: Solid-state NMR studies and DFT calculations, J. Phys. Chem. C **127**, 14303 (2023).

[24] J. Cízek, I. Procházka, F. Becvár, R. Kuzel, M. Cieslar, G. Brauer, W. Anwand, R. Kirchheim, and A. Pundt, Hydrogen-induced defects in bulk niobium, Phys. Rev. B **69**, 224106 (2004).

[25] J. Cízek, I. Procházka, S. Daniš, G. Brauer, and W. Anwand, R. Gemma, E. Nikitin, R. Kirchheim, A. Pundt, and R. K. Islamgaliev, Hydrogen-vacancy complexes in electron-irradiated niobium, Phys. Rev. B **79**, 054108 (2009).

[26] B. L. Shivachev, T. Troev, and T. Yoshiie, Positron lifetime computations of defects in nickel containing hydrogen or helium, J. Nucl. Mater. **306**, 105 (2002).

[27] K. Sato, A. Hirosako, K. Ishibashi, Y. Miura, Q. Xu, M. Onoue, Y. Fukutoku, T. Onitsuka, M. Hatakeyama, S. Sunada, and T. Yoshiie, Quantitative evaluation of hydrogen atoms trapped at single vacancies in tungsten using positron annihilation lifetime measurements: Experiments and theoretical calculations, J. Nucl. Mater. **496**, 9 (2017).

[28] G. Colombi, R. Stigter, D. Chaykina, S. Banerjee, A. P. M. Kentgens, S. W. H. Eijt, B. Dam, and G. A. de Wijs, Energy, metastability, and optical properties of anion-disordered REO_xH_{3-2x} (RE = Y, La) oxyhydrides: A computational study, Phys. Rev. B **105**, 054208 (2022).

[29] H. Leegwater, H. Schut, W. Egger, A. Baldi, B. Dam, and S. W. H. Eijt, Divacancies and the hydrogenation of Mg-Ti films with short range chemical order, Appl. Phys. Lett. **96**, 121902 (2010).

[30] S. J. Tao, Positronium annihilation in molecular substances, J. Chem. Phys. **56**, 5499 (1972).

[31] M. Eldrup, D. Lightbody, and J. N. Sherwood, The temperature-dependence of positron lifetimes in solid pivalic acid, Chem. Phys. **63**, 51 (1981).

[32] D. Chaykina, T. de Krom, G. Colombi, H. Schreuders, A. Suter, T. Prokscha, B. Dam, and S. Eijt, Structural properties and anion dynamics of yttrium dihydride and photochromic oxyhydride thin films examined by *in situ* μ^+SR, Phys. Rev. B **103**, 224106 (2021).

[33] Y. Komatsu, R. Shimizu, R. Sato, M. Wilde, K. Nishio, T. Katase, D. Matsumura, H. Saitoh, M. Miyauchi, J. R. Adelman, R. M. L. McFadden, D. Fujimoto, J. O. Ticknor, M. Stachura, I. McKenzie, G. D. Morris, W. Andrew MacFarlane, J. Sugiyama, K. Fukutani, S. Tsuneyuki, and T. Hitosugi, Repeatable photoinduced insulator-to-metal transition in yttrium oxyhydride epitaxial thin films, Chem. Mater. **34**, 3616 (2022).

[34] J. Chai, Z. Shao, H. Wang, C. Ming, W. Oh, T. Ye, Y. Zhang, X. Cao, P. Jin, S. Zhang, and Y. Sun, Ultrafast processes in photochromic material YH_xO_y studied by excited-state density functional theory simulation, Sci. China Mater. **63**, 1579 (2020).

[35] R. Stigter, A Computational Investigation on the Structure of Yttrium Oxyhydride Compounds and Their Anion Mobility, MSc thesis (Delft University of Technology, Delft, The Netherlands, 2020).

[36] P. Hautojarvi, Defects in semiconductors-recent progress in positron experiments, Mater. Sci. Forum **175**, 47 (1995).

[37] G. Brauer, W. Anwand, P. G. Coleman, J. Stormer, F. Plazaola, J. M. Campillo, Y. Pacaud, and W. Skorupa, Post-implantation annealing of SiC studied by slow-positron spectroscopies, J. Phys.: Condens Matter **10**, 1147 (1998).

[38] This value is calculated based on the composition $YH_2O_{0.5}$. In this composition, three of the six closest octahedral sites of yttrium are occupied by hydrogen. Assuming that 10% of the octahedral hydrogen from all previously occupied octahedral sites is removed, the probability of removing one of the three hydrogen atoms from the nearest-neighbor octahedral sites of the yttrium is approximately 25%$(1 - (0.9)^3 \approx 0.27)$.

[39] J. Montero, F. A. Martinsen, M. Garcia-Tecedor, S. Z. Karazhanov, D. Maestre, B. Hauback, and E. S. Marstein, Photochromic mechanism in oxygen-containing yttrium hydride thin films: An optical perspective, Phys. Rev. B **95**, 201301(R) (2017).

[40] K. Fukui, S. Limura, T. Tada, S. Fujitsu, M. Sasase, H. Tamatsukuri, T. Honda, K. Ikeda, T. Otomo, and H. Hosono, Characteristic fast H ion conduction in oxygen-substituted lanthanum hydride, Nat. Commun. **10**, 2578 (2019).

[41] K. Fukui, S. Iimura, J. J. Wang, T. Tada, T. Honda, K. Ikeda, T. Otomo, and H. Hosono, Stabilization factor of anion-excess fluorite phase for fast anion conduction, Chem. Mater. **33**, 1867 (2021).

[42] J. Crank, *The Mathematics of Diffusion*, 2nd ed. (Oxford University Press, London, 1975).

[43] E. Haurat, J. P. Crocombette, T. Schuler, and M. Tupin, Hydrogen diffusion coefficient in monoclinic zirconia in presence of oxygen vacancies, Int. J. Hydrogen Energy **47**, 33517 (2022).

[44] N. Fernandez, Y. Ferro, and D. Kato, Hydrogen diffusion and vacancies formation in tungsten: Density functional theory calculations and statistical models, Acta Mater. **94**, 307 (2015).

[45] A. Bikowski and K. Ellmer, A comparative study of electronic and structural properties of polycrystalline and epitaxial magnetron-sputtered ZnO:Al and $Zn_{1-x}Mg_xO$:Al films-Origin of the grain barrier traps, J. Appl. Phys. **114**, 063709 (2013).

[46] C. Mitra, P. Raychaudhuri, J. John, S. K. Dhar, A. K. Nigam, and R. Pinto, Growth of epitaxial and polycrystalline thin films of the electron doped system $La_{1-x}Ce_xMnO_3$ through pulsed laser deposition, J. Appl. Phys. **89**, 524 (2001).

[47] K. Hayashi, Kinetics of electron decay in hydride ion-doped mayenite, J. Phys. Chem. C **115**, 11003 (2011).

[48] K. Hayashi, P. V. Sushko, Y. Hashimoto, A. L. Shluger, and H. Hosono, Hydride ions in oxide hosts hidden by hydroxide ions, Nat. Commun. **5**, 3515 (2014).

[49] K. Hayashi, S. Matsuishi, T. Kamiya, M. Hirano, and H. Hosono, Light-induced conversion of an insulating refractory oxide into a persistent electronic conductor, Nature (London) **419**, 462 (2002).

[50] M. Torrent, F. Jollet, F. Bottin, G. Zérah, and X. Gonze, Implementation of the projector augmented-wave method in the ABINIT code: Application to the study of iron under pressure, Comput. Mater. Sci. **42**, 337 (2008).

[51] B. Barbiellini, M. J. Puska, T. Torsti, and R. M. Nieminen, Gradient correction for positron states in solids, Phys. Rev. B **51**, 7341 (1995).

[52] N. A. W. Holzwarth, A. R. Tackett, and G. E. Matthews, A Projector Augmented Wave (PAW) code for electronic structure calculations, Part I: Atompaw for generating atom-centered functions, Comput. Phys. Commun. **135**, 329 (2001).

[53] S. Goedecker, M. Teter, and J. Hutter, Separable dual-space Gaussian pseudopotentials, Phys. Rev. B **54**, 1703 (1996).

[54] E. Boronski and R. M. Nieminen, Electron-positron density-functional theory, Phys. Rev. B **34**, 3820 (1986).

[55] J. P. Perdew, K. Burke, and M. Ernzerhof, Generalized gradient approximation made simple, Phys. Rev. Lett. **77**, 3865 (1996).